nature astronomy

Article
https://doi.org/10.1038/s41550-023-02122-6

Detection of long-lasting aurora-like radio emission above a sunspot

In the format provided by the authors and unedited

Supplementary information

Variability of the radio emission over a solar rotation

Extended Data Fig. 3 shows the time history of the solar radio and X-ray emission for an entire solar rotation period. The temporal and spectral variation of the radio emission indicates that the same coherent emission feature persists for over an entire week (or ∼1/4 of the rotation period; demarcated by the yellow shaded area in Extended Data Fig. 3b, d–e). The HMI continuum image series in Extended Data Fig. 3a show that AR 12529, which the sunspot belongs to, is the only AR on the disk when the sunspot radio emission is present, therefore we attributed the impulsive X-ray emission shown in Extended Data Fig. 3e to the flare activity in this AR. The GOES X-ray flux level displays sporadic flare activity during the time when the sunspot moves across the solar disk, and drops to the background level after the sunspot moves to the back side of the Sun. The radio emission shows little correlation with that of the X-ray emission from flare activity in the AR. In fact, the radio emission is only visible for a limited duration during the rotation cycle, specifically when the sunspot is located between longitudes of -70° to -10°. The temporal, spectral, and polarization characteristics of the radio emission, including broadband arc-like structures in the time-frequency domain (Extended Data Fig. 3f), closely resemble ECM emissions reported in the literature from (sub)stellar systems[1,2]. Most notably, the sun-as-a-star light curves throughout a solar rotation, primarily modulated by the coherent sunspot radio bursts (Extended Data Fig. 3c–d), display a striking similarity to rotationally-modulated periodic radio aurora from M-dwarfs[3]. The similarity is mainly evident in the temporal patterns in radio emissions. In both cases, the radio emissions exhibit rotationally modulated behavior, which corresponds to the rotation of the respective celestial bodies. Specifically, in the solar case, the burst duty cycle—the fraction of time spent in bursting—is approximately 20% in the L and P bands. This value is comparable to those of coherent radio bursts observed in M-dwarfs within the same frequency range, as demonstrated in previously reported stellar instances.[3,4].

Emission mechanism of the sunspot radio bursts

There are two major competing emission mechanisms that can generate coherent radio emissions in the solar corona. Coherent plasma radiation often dominates the solar radio emission of solar flares in a wide frequency range spanning from ~ 1 GHz all the way to tens of MHz. They are driven by the non-linear growth of plasma instabilities and followed by a wave-wave conversion, radiating at a frequency close to the fundamental or second harmonic electron plasma frequency $\nu_{\rm pe} \approx 8980\sqrt{n_e}$ Hz. In contrast, the electron cyclotron maser (ECM) emission likely dominates the emission in regions of high magnetic field strength and/or low plasma density, where the electron plasma frequency ($\nu_{\rm pe}$) is less than the electron gyrofrequency ($\nu_{\rm ce}$) at the source site[5]. The ECM mechanism has been suggested as the primary emission mechanism of auroral radio emission in planetary magnetospheres, such as the terrestrial auroral kilometric radiation[6], Jovian decametric radiation[7], and Saturn's kilometric radiation[8], as well as strong radio radiation with high circular polarization in a variety of magnetically active stars such as M dwarfs[1,9,10]. ECM emission is generated near low harmonics of the electron cyclotron frequency $s\nu_{\rm ce} = 2.8 \times 10^6 sB\,$Hz (where s is the harmonic number and B is the magnetic field strength in Gauss) due to non-linear wave growth under a variety of plasma instabilities including loss-cone, ring shell, or horseshoe instabilities[11]. We recognize that details of the ECM model, including the responsible plasma instability, local driver of ECM (e.g., a parallel electric field, as suggested by Ergun et al. 2000[12]), and energy efficiency of the ECM emission remain largely unexplored. Addressing these details requires further, and preferably, *in situ* measurements to characterize the local magnetic and electric field, electron momentum and angular distribution, and other plasma parameters at the radio emitter[12].

Although establishing a comprehensive emission model is challenging and beyond the scope of the current study due to a lack of in situ data, we can investigate the emission mechanism using remote-sensing data provided by multi-wavelength observations. By employing a data-constrained 3D coronal magnetic field model and electron number density model, we calculate the ratio $R = \nu_{\rm pe}/\nu_{\rm ce}$ in the 3D volume above the active region to identify regions more likely for the plasma radiation or ECM emission. The method has been previously employed to investigate the emission mechanism of coherent radio bursts in the solar corona[13,14]. The resulting distributions of $\nu_{\rm pe}$, $\nu_{\rm ce}$, and their ratio R at the $Y = 0$ plane in the model are shown, respectively, in the left column of Extended Data Fig. 5. Although both the electron number density n_e and magnetic field strengths B decrease with increasing height in the corona, and so do the plasma frequency $\nu_{\rm pe}$ and cyclotron frequency $\nu_{\rm ce}$, the B decreases more rapidly in the region above the sunspot. This leads to a low R cavity just above the sunspot (Extended Data Fig. 5c), in which the electron maser instability is likely to be excited. The ECM emission frequency ν in the $R \lesssim 1$ cavity ranges from above 1.5 GHz to 250 MHz (Extended Data Fig. 5b). This agrees with the observations that the sunspot auroral bursts are presented in a wide frequency range from ~ 2 GHz all the way to the lowest frequency of RSTN at 245 MHz (Extended Data Fig. 2a). We acknowledge that n_e and $\nu_{\rm pe}$ are reliant on the column depth D, which should be regarded as a rough estimate. Nevertheless, it is important to note that the electron plasma frequency gradually varies with the fourth root of column depth D, following the relationship $\nu_{\rm pe} \propto n_e^{0.5} \propto 1/D^{0.25}$. Consequently, changes in D have only a minimal impact on the electron plasma frequency ν_{pe}. Varying D from 15 to 150 Mm leads to a 30% difference in ν_{pe} with respect to the value derived using $D = 50$ Mm (Supplementary Fig. 4c). This variation does not significantly affect the inferred ECM harmonic and the ratio R.

Owing to the relatively high plasma density in the solar corona compared to, e.g., planetary magnetospheres, the detectability of the ECM emission is also affected by gyro-resonant absorption due to the ambient thermal plasma at higher harmonics of the electron gyro-frequency[5]. The opacity of the gyro-resonance layers depends on the magnetic field geometry, the thermal electron number density n_e and the viewing direction[15]:

$$\tau(s,\nu,\theta) = \frac{\pi e^2}{2m_e c}\frac{n_e L_B(\theta)}{\nu}\frac{s^2}{s!}\left(\frac{s^2}{2\mu}\right)^{s-1} F(\theta) \tag{1}$$

where θ is the angle between the LOS and the local magnetic field direction, $L_B(\theta) = B/|\nabla B|$ is the magnetic scale height along the LOS direction, $\mu = m_e c^2/k_B T$ is the square of the ratio between the speed of light and electron thermal speed, and $F(\theta)$ is a function of angle θ:

$$F(\theta) = \frac{\sin^{2s-2}\theta\left(\sin^2\theta + 2s\cos^2\theta + \sigma\sqrt{\sin^4\theta + 4s^2\cos^2\theta}\right)^2}{\sin^4\theta + 4s^2\cos^2\theta + \sigma\sin^2\theta\sqrt{\sin^4\theta + 4s^2\cos^2\theta}} \tag{2}$$

with $\sigma = 1$ for extraordinary mode (X mode) or $\sigma = -1$ for ordinary mode (O mode).

The nearly 100% right circularly polarized radio emission is closely associated with the sunspot in negative magnetic polarity, suggests that the emission is likely in the ordinary mode, or O mode. With Equation 1, we evaluate the absorption of ECM radiation produced at a harmonic of s_e by the overlying gyro-resonance layer at $s_a = s_e + 1$ (the absorption at larger harmonics is much smaller and can be neglected) for a given observing frequency ν. In Extended Data Fig. 5d–f, we show, respectively, maps of L_B, θ and the opacity τ of the $s_a = 1, 2, 3$ layer for o-mode radiation at a representative frequency of $\nu_{\text{GHz}} = 1.0$ along the line of sight at the $Y = 0$ plane. Our model shows that the $s_a = 2$ layer is mostly optically thick except for a narrow window at small θ values with respect to the line of sight where the ECM emission produced at the fundamental harmonic $s_e = 1$ can escape. On the other hand, the model suggests that ECM emission produced at the second harmonic $s_e = 2$ is only partially affected by the gyro-resonance absorption layer at $s_a = 3$. The latter shows a morphology similar to the $s_a = 2$ layer, but has a much wider transparent window covering the sunspot umbra and penumbra regions. Therefore, the second-harmonic ECM emission can escape from the transparent window in the $s_a = 3$ layer and be observed, as demonstrated in the schematic picture in Fig. 4h. We note that while the opacity structure model is dependent linearly on electron number density n_e, the latter varies with the square root of column depth D. Changes in D only have a minimal impact on opacity structure, following the relationship $\tau \propto D^{-0.5}$. Varying D from 15 to 150 Mm results in a scale factor of 0.7 to 2.2 for the opacity value, which is not significant enough to affect the overall opacity structure for the ECM emission and its observability (Supplementary Fig. 5).

We end this section with a brief discussion of the growth of ECM emission in X and O mode, which depends heavily on the value of $R = \nu_{\text{pe}}/\nu_{\text{ce}}$. Parametric investigations on ECM instability in the literature suggests that at the fundamental O mode or second harmonic X mode radiation would be dominant when $0.3 \lesssim R \lesssim 1$, and the second harmonic O-mode would dominate the radiation when $1.4 \lesssim R \lesssim 2$[16,17]. In the regions where the radio source at 1–2 GHz, the ratio R derived from the magnetic field model and coronal density model generally falls in the range of $0.3 \lesssim R \lesssim 1$ (Extended Data Fig. 5b), which would favor fundamental O mode or second harmonic X mode. However, as we described in the coronal density model section, the corona density depends strongly on the selection of the column depth. The absolute coronal density can be scaled up by a factor of a few if we assumed a smaller column depth, so that the ratio R can satisfy required values for second harmonic O mode to dominate. We caution that such uncertainty in the density model impedes an accurate determination of the ratio R, so as for the preferable emission wave mode. For emission below 1 GHz, we choose not to discuss the wave mode because of lacking imaging observation and polarization measurement at frequencies below 1 GHz. Nevertheless, Chen et al[18] found the corona may consist of many unresolved overdense loops based on the discrepancy between the density inferred from the frequency of type III radio bursts and that inferred from EUV observations. It is suggested that there are overdense magnetic loops above the sunspot with a density enhancement by up to an order of magnitude against the tenuous background, the ratio R in which can be greater by the square root of the same factor. If the observed coherent radio bursts can be interpreted as ECM emission originating in these overdense loops, the second harmonic O mode radiation would be more probable to dominate in these loops with a higher plasma density. The overdense loops scenario offers an alternative avenue for second harmonic O mode ECM radiation to dominate in a general low R environment (R<1).

Spatial distribution of the ECM source

With spatially and temporally resolved imaging spectroscopy, we can derive the centroid location of each observed source at any given time t and frequency ν, provided that it has a sufficient signal-to-noise-ratio against the quiescent background. The top panels in Extended Data Fig. 6 shows examples of the distribution of the frequency-dependent source centroid locations for seven individual 20-second time integrations. Intriguingly, the spatial distribution of each burst forms a close-to-linear distribution in a way similar to those derived from electron-beam-driven type III radio bursts[18,19].

As the emission frequency ν due to the ECM mechanism depends only on the magnetic field strength B, the observed spatial distribution of the radio source centroid location at a given frequency ν in projection $\vec{r}(\nu)$ is governed by the magnetic field distribution above the sunspot $\vec{r}(B)$. Our observations have suggested that, for each radio burst, the distribution of the frequency-dependent radio source centroids is likely aligned with a single magnetic loop. Therefore, we can reduce the distribution of the radio sources to a one-dimensional dependence of $d(\nu)$, where d denotes the plane-of-the-sky projected distance from a reference location along the respective loop, selected as that of the source centroid at 1 GHz. We construct the $d(\nu)$ dependence of the seven example times, shown in the bottom panel of Extended Data Fig. 6 as colored circles (whose sizes are scaled by their peak flux). With the 3D coronal magnetic field model to provide the mapping of $d(B)$ for each magnetic loop in projection, we can predict the expected $d(\nu)$ dependence in different viewing angles of θ. In the bottom panel in Extended Data Fig. 6, we show the predicted $d(\nu)$ dependence along three directions with θ equals to 30°, 45°, and 60° as the dotted, solid, and dashed lines, respectively. The results suggest that the viewing angle θ of the radio sources with the observed $d(\nu)$ dependence should lie in the range of 30°–60°. This range of viewing angles demarcates a region in the vicinity of the apex of the $s = 2$ gyroresonance dome (denoted as the green contour in Extended Data Fig. 5e&f), corresponding to the predicted ECM emission sites that are co-spatial with the transparent window of the $s_a = 3$ gyroresonance layer in projection. The range of viewing angles is also consistent with the values of θ in the inferred source region (green contour in Extended Data Fig. 5e.) We note that the beaming angle of 30°–60° is generally smaller than observed values (75°–80°) in the case of Jovian radio auroral radiation[20], but similar to the beaming angles ($\gtrsim 40°$) of the auroral kilometric radiation in the terrestrial case[12]. The latter is often attribute to the refraction effect that the radio waves is initially emitted to the perpendicular direction but is ducted away through refraction at the borders of the density depletion cavity in which the emission is produced[12]. This does not seem to be the case for the sunspot radio emission. For the ducting to occur, the plasma frequency of the surrounding boundary of the low-density cavity should be significantly higher than the emitting frequency of the radiation. This requires a plasma density of at least a few times of $10^{10}\,\mathrm{cm}^{-3}$, which is much higher than the inferred plasma density near the source region. One possibility is that the small beaming angle is a result of ECM processes coupled with Alfvén waves. Wu et al (2012)[21] found that preexisting Alfvén waves can modify the classical ECM processes by affecting the velocity distribution of energetic electrons via pitch-angle scattering. Indeed, Alfvén waves is expected in the quiet solar corona[22,23] and flare regions[24]. The beaming angle of second harmonic O mode ECM emission, if driven by nonthermal electrons in a horseshoe distribution, can be as low as 30°. The interpretation of the observed coherent radio bursts as second harmonic O mode ECM emission is consistent with the small beam opening angles predicted in the analyticla study[17]. Nevertheless, we acknowledge that the observed beaming angle is not fully consistent with the values of previously observed planetary ECM emissions. To produce a fully self-consistent model of ECM emission from the sunspot requires not only a better understanding the corona context using a data constrained MHD model, but also a fully kinetic simulations to achieve a realistic nonthermal electron distribution, both of which are beyond the scope of this study.

On the other hand, plasma emission radiates at a frequency close to the fundamental or second harmonic electron plasma frequency $\nu_{\rm pe}$. Plasma radiation at frequencies in the range 1-1.5 GHz suggests the ambient plasma density above the sunspot in the range $1\text{–}3 \times 10^{10}\,\mathrm{cm}^{-3}$, which is more than an order of magnitude higher than coronal density model constrained by the DEM analysis (Supplementary Fig. 4c). It is worth asking, however, whether the observed radio bursts are plasma radiation originating from the aforementioned overdense magnetic loops in the corona. As the emission frequency ν due to the plasma radiation mechanism is proportional to the square root of plasma density ($\nu_{\rm pe} \propto \sqrt{n_{\rm e}}$), the $d(\nu)$ of the plasma radiation source is determined by the plasma density distribution above the sunspot. The plasma frequency ν varies from 1.0 to 1.5 GHz over $d(\nu)$ of 3–6 Mm corresponds to the plasma density varying from 1×10^{10} to $3 \times 10^{10}\,\mathrm{cm}^{-3}$ over a height of 4–8 Mm, assuming the overdense loops have inclination angles of $\sim 45°$. This is equivalent to a density scale height $\mathrm{L}_n = n_{\rm e}/(dn_{\rm e}/d\vec{r})$ of 4–8 Mm under hydrostatic equilibrium, which are at least an order of magnitude smaller than the hydrostatic value at typical coronal temperature ($\mathrm{L}_n \approx 46T_{\rm MK}\,\mathrm{Mm}$, or 94 Mm for $T = 2\,\mathrm{MK}$[25]). Such steep density profiles, in other words, steep pressure gradients, are inconsistent with the expectation for the quasi-static magnetic structures above the sunspot. Therefore, we reaffirm the conclusion that plasma radiation is unlikely the responsible mechanism for the observed radio bursts.

Observability of the sunspot ECM emission

ECM generates radiation along a thin, conical sheet. Consequently, sunspot ECM emissions are only observable when the narrow radiation beam crosses the line of sight due to the Sun's rotation. Although ECM emissions should also appear when the sunspot is in the symmetric phase on the western side of the solar disk, they are only visible for a specific heliocentric angle range on the eastern side, as shown in Extended Data Fig. 3. In this study, we attribute this phenomenon to the influence of solar flares on the observability of sunspot ECM emissions. During the observed sunspot radio bursts, the emission source region was far from the flare sites. However, as the sunspot rotates to the other side of the solar disk, the potential emission source (the green contour line in Supplementary Fig. 6) would become much closer to the flare sites. The close spatial proximity of source sites to flares can significantly alter the local plasma and magnetic environment, affecting ECM generation and escape. A more detailed discussion of various impacts is provided below:

- ECM condition: The ECM mechanism requires a specific condition of $R \lesssim 1$ at the source site[5]. Given the source site's proximity to flares, the impact of solar flares on coronal density structures must be considered. The thermal plasma density distribution during flares is highly dynamic and complicated, which required specialized modeling efforts to simulate its temporal evolution[26]. While this is beyond the scope of this study, a rough estimate can still be performed. Solar flares can increase coronal plasma density by a factor of over 10 within tens of seconds[27]. This over 10-fold increase in density near flare regions could raise the R value in the nearby ECM source region by a factor of a few, as R is proportional to $\sqrt{n_e}/B$. In this case, the source region near the flare sites may not meet the ECM condition and cannot produce ECM emission.

- Opacity: The solar corona's highly structured nature means that the opacity of the gyro-resonance absorption layer, which depends on the viewing direction and 3D distributions of the coronal magnetic field and thermal plasma[5], will change over time as the Sun rotates. This change subsequently affects the emissivity and polarization of sunspot ECM emissions. As mentioned earlier, the opacity varies linearly with the electron number density n_e. A more than 10-fold increase in n_e near the flare regions could significantly alter the opacity of the nearby gyro-resonance layer in the line of sight (Supplementary Fig. 6), restricting the escape of ECM radiation.

- Magnetic configuration: In our interpretation, the generation of the sunspot radio bursts requires closed magnetic loops trapping energetic electrons. Recurring non-eruptive flares are favored because they can continuously replenish the population of energetic electrons in the overarching radio-hosting magnetic field lines above the energy release site without disrupting the overall magnetic field geometry. In contrast, eruptive flares are expected to open up the magnetic field lines above[28]. The newly accelerated electrons by solar flares can easily escape to interplanetary space along the opened field lines without getting trapped in the low corona. Moreover, the opening of the overarching magnetic field lines results in the destruction of the electron reservoir where energetic electrons accelerated by previous flares are trapped, further interrupting the generation of the sunspot radio bursts. As demonstrated in Extended Data Fig. 3(e), NOAA 12529 AR became more violent on 2016 April 14, producing an M class flare and a few sub-M class flares. In contrast, the AR only produced a few C class flares earlier.

One or more of the factors mentioned above may influence the observability of the sunspot ECM emission as the viewing angle varies, in addition to the effect of stellar rotation. Understanding the viewing geometry effects requires long-term broadband dynamic imaging spectropolarimetry to study in detail the time-dependent variations of the morphology, location, and polarization of the radio source. The emissivity of sunspot coherent radiation, including but not limited to the emission intensity, polarization and wave mode, depends heavily on the magnetic field distribution and coronal plasma distribution, which are subjected to change with time due to the gradual evolution of the radio-hosting active region and abrupt energy release events. To establish the relationships of coherent radio bursts with the structure and dynamics of the corona, including plasma density inhomogeneity, magnetic field topologies, and their variations, broadband dynamic imaging spectroscopy observations in the frequency range of 200 MHz to 2 GHz are required. These observations should be complemented by other multi-wavelength observations, including optical, EUV, and X-ray. Moreover, with the aid of data-constrained coronal 3D magnetic and thermodynamic structure, imaging spectropolarimetry would allow us to characterize and constrain coronal thermal parameters, magnetic field properties, and the energy distribution of nonthermal electrons that drive ECM emission. Detailed context data at other wavelengths, coupled with radio imaging observations, would enable the examination of the relationship between the rotational modulations of sunspot ECM emission and other significant observables, such as photometric and Doppler spectroscopic measurements[29,30]. Such observations will be crucial for improving our understanding of the generation and rotational modulation effects of ECM bursts from the Sun and other stars.

An important corollary to the discussion of observability of the sunspot ECM emission is the potential influence of viewing effects on the duty cycle of stellar ECM emissions. If these stellar emissions were associated with the presence of starspots on the surfaces of these (sub)stellar systems, viewing effects may play a role in determining the temporal pattern within a single duty cycle of these emissions. Like the solar case, many previously reported stellar ECM emissions only appear in a certain range of stellar rotational phase[30,31]. Depending on the relative positions of the starspot and its neighboring flare sites with respect to the light of sight, as well as the inclination of the rotation axis relative to the line of sight as viewed from the Earth, stellar ECM emissions may manifest a second time in symmetric phase with respect to the stellar-centric 0° longitude line. Similar cases have also been observed in other stars[3,32]. Furthermore, as a type of transient radio source, the duty cycle of stellar ECM emissions could also vary as a consequence of the short-term evolution of the starspot and its magnetic connectivity to other parts of the stellar surface. Long-term variations, such as the emergence of a starspot, may lead to the appearance of ECM radio emission on a star that previously lacked such radio bursts in earlier observations, and vice versa. Understanding these viewing effects and their impact on the observability of sunspot and starspot ECM emissions can inform future survey-type observations of stellar ECM emissions.

In concluding this section, we explore the potential applicability of our model to early-type stars (spectral type B or A). Rotationally modulated ECME emissions have been discovered in several early-type stars, exhibiting consistent phases over extended periods[30,32]. The prevailing hypothesis suggests that global dipole-like magnetic fields can create magnetic-mirror-like conditions necessary for maser emission[33]. These stars often possess magnetic fields with kG strengths and simple topologies, often well approximated by a dipole[34]. Stellar wind[32] or magnetic reconnection in the magnetosphere[35] may provide energetic electrons required to drive ECM emissions. These electrons then become trapped in the stellar magnetospheric pole regions, producing magnetic-mirror-like conditions that facilitate ECME emission. However, recent studies reveal that radio ECM emission can emerge from stars with surface magnetic fields significantly deviating from an axisymmetric dipole[36], leaving the role of the dipole magnetic field topology in producing radio ECM emission remains an open question. Analogous to the magnetospheric pole regions and the electromagnetic engine in the magnetosphere, a localized magnetic structure such as a starspot and nearby flare activity can also produce radio ECM emissions, similar to the solar case. Recent time-series photometry from space missions like Kepler, K2, and TESS challenges this belief, suggesting that rotational modulation is probable in stars with radiative envelopes[37]. The observed light variations can be most simply interpreted as rotational modulation induced by surface brightness inhomogeneities, such as magnetic spots. These localized magnetic fields might be associated with magnetic fields generated in subsurface convection zones[38]. Additionally, it is plausible that differential rotation in A and B stars may be sufficient to create local magnetic fields via dynamo action[39]. Due to the extreme stability of the magnetic fields in these types of stars[40], the periodic ECME emission can be remarkably stable, unlike the case for the highly dynamic magnetic field of the Sun. If the rotational modulation observed in early-type stars indeed results from persistent magnetic spots, our model could offer an alternative approach to generating a stable burst duty cycle over extended periods in these stars. However, this proposition depends on the presence of persistent magnetic spots on early-type stars. Further investigation is necessary to assess the efficacy of the model in accounting for the long-term radio emission behavior exhibited by these stars.

Source size and brightness temperature

The broadband radio bursts emitting from the sunspot are detectable across frequencies ranging from 245 MHz to 1.7 GHz. The maximum flux density of these recorded bursts in stokes I, observed at 245 MHz at approximately 23 UT on April 12, is around 2000 sfu, or 2×10^{10} mJy. Were the observed bursts to be viewed from a stellar distance, the flux density at 245 MHz can be expressed as $0.5(D_{\rm pc})^{-2}$ mJy, where D_{pc} is the stellar distance in parsec. If we take the median distance of 20 parsec in the recent LOFAR observations[41], the flux density would approximate 1 μJy. Although the total flux density is two or three orders of magnitude lower than the median values reported in the recent LOFAR observations at hundreds of MHz[41], we argue that the brightness temperature of the sunspot radio source can still be very high. This is owing to the likely compact and unresolved nature of many individual bursts that comprise the observed radio source. We consider the magnetic loops anchored at the sunspot where impulsively accelerated electrons are injected and an unstable loss-cone distribution is set up by magnetic mirroring on the sunspot end of the loops. the brightness temperature for a continuously operating maser is given by[5],

$$T_{\rm b} = \frac{m_e v_0^2}{4\pi k_{\rm B}} \frac{c^2}{\nu^2 L r_0} \approx 2\times10^{12} \left(\frac{E}{1\ \rm keV}\right) \left(\frac{\nu}{200\ \rm MHz}\right)^{-2} \left(\frac{L}{R_\odot}\right)^{-1}\ \rm K \tag{3}$$

where v_0 is the velocity of the emitting electrons, ν is the emission frequency, L is the length scale of the magnetic trap with respect to the solar radius $R_\odot$, r_0 is the classical electron radius, m_e is the electron mass, $k_{\rm B}$ is the Boltzmann constant, and c is the speed of light. Using a magnetic loop length scale of approximately 1/10 of the solar radius $R_\odot$ and electron energy E of 20 keV, the brightness temperature is estimated to be approximately 10^{14} K at 245 MHz and 10^{13} K at 1 GHz for the fundamental emission. For the second harmonic ECM emission, the values are 10^{12} K at 245 MHz and 10^{11} K at 1 GHz, considering the latter's growth rate potentially being two orders of magnitude lower than the fundamental[17].

High brightness temperatures are not uncommon for solar radio bursts, as evidenced by solar decimetric spikes[42] whose source size scale is suggested to be below 1000 km. For the 20 sfu radio observed by VLA at 1 GHz, the brightness temperature corresponds to a source size of 1000×1000 km. Since the observed radio source of the 1 GHz image is marginally resolved by VLA, a single 1000×1000 km source can not account for the asymmetric structure seen in the VLA 1 GHz image. We speculate that the observed radio source may comprise many small, unresolved sources instead of a single 1000×1000 km source. To illustrate such a possibility, we employed a hundred ($N = 100$) randomly distributed 10^{11} K point sources in the second harmonic gyroresonance of $\nu_{\rm GHz} = 1$ at selected field lines. We note that the choice of the source number N is arbitrary, but it does not affect our subsequent analysis. Each point source has a uniform diameter of $1000/\sqrt{N}$ km and a flux density of $20/N$ sfu. The model is shown in Supplementary Fig. 2a. The input model is first convolved with a $40''$ Gaussian beam to account for angular scattering at 1 GHz by coronal turbulence[43]. Subsequently, the model is convolved with the synthesis beam of the VLA at 22 UT on April 9 to create a simulated VLA image. The result, shown in Supplementary Fig. 2b, qualitatively agrees with the actual VLA image at this frequency in terms of source location and size. It is important to note that the argument for multiple sources is consistent with the inhomogeneous and fragmentary nature of magnetic reconnection, as evidenced by recent VLA solar observations[19]. Under this scenario, semi-relativistic electron beams can be emanated into distinct field lines, even though they are accelerated within an extremely compact region (~ 600 km) in the low solar corona over a brief time scale (1–2 seconds). Assuming that each ECM source is associated with a different electron beam energized within the same acceleration region, they can, in principle, arrive at various field lines above the sunspot, resulting in the scattered distribution of ECM sources as portrayed in the model. While our observations show that the radio bursts could originate from numerous distinct magnetic field lines, we note that these field lines are all rooted at the umbra region of the sunspot with a negative polarity. Consequently, at any particular instance, these field lines share similar line-of-sight angles with regard to the observer, which gives rise to a high degree of circular polarization of the bursts over our observational period of several hours.

Nevertheless, explaining the observed radio bursts on certain M dwarfs with orders of magnitude higher flux density than our case remains challenging. However, we note that the plasma environment on these stars are much more extreme than that on the Sun. First, the average surface magnetic field on these stars can exceed kilo Gauss[44–46], compared to $\sim$1–10 Gauss on the Sun. The magnetic fields in these starspots may exceed those in sunspots by orders of magnitude, potentially boosting the intrinsic brightness of the ECM emission[47]. Second, the level of flare activity on these fully convective stars is much higher than that on the Sun, allowing a possibility to pertain a much larger spatial and temporal filling factor for these bursts over the stellar disk. This speculation is reflected in the radio/X-ray correlation in the context of the GB relation, where the sunspot radio source exhibits similar deviation from the radio/X-ray relation as other stellar radio ECM emissions, despite its relatively low magnetic activity level (X-ray luminosity) among the others. Both may potentially contribute to the much brighter bursts observed on these active stars, although further observational, theoretical, and modeling investigations are required.

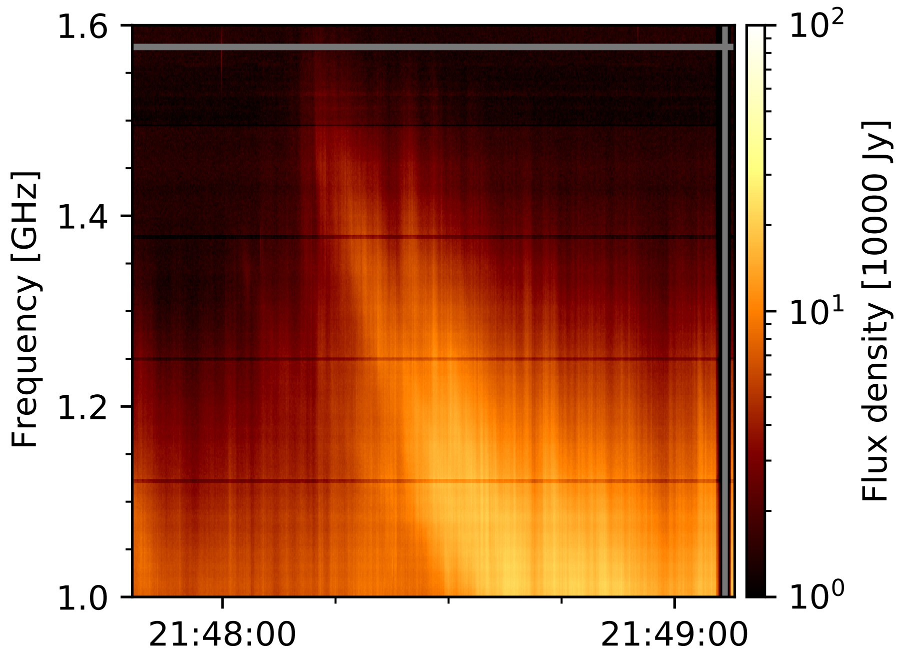

Supplementary Fig. 1. **Details of the dynamic spectrum between 21:48 and 21:49 UT on April 9, 2016.** The format is the same as Extended Data Fig. 1 in the Methods section.

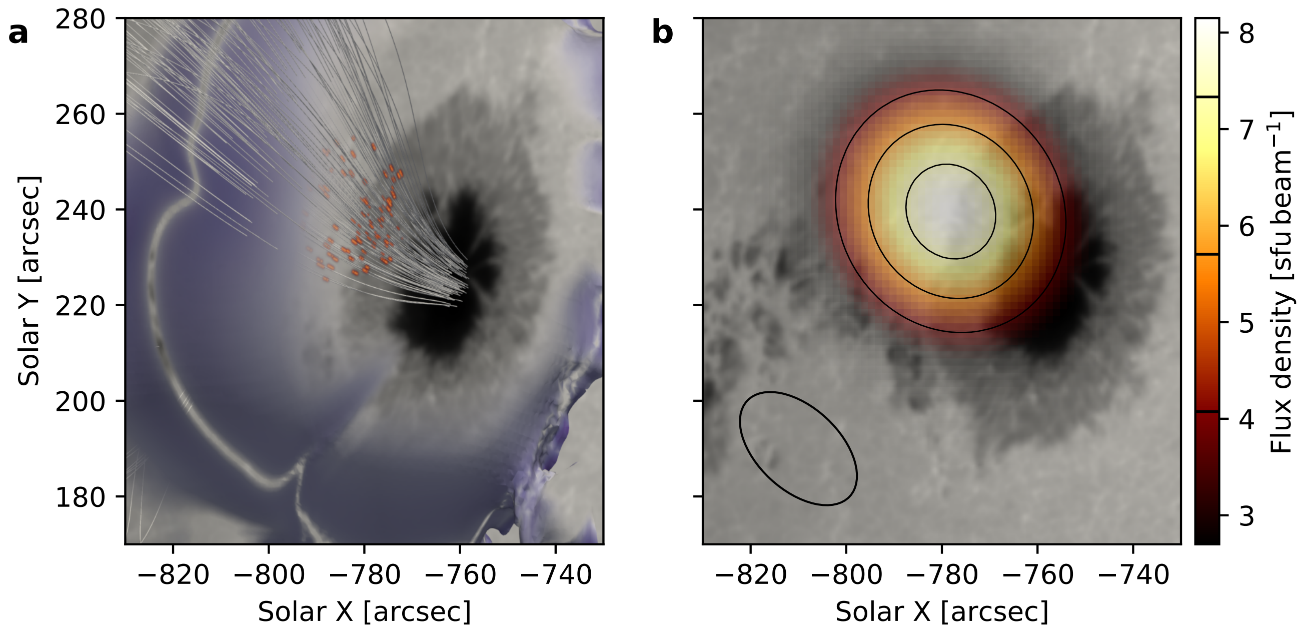

Supplementary Fig. 2. **Simulation of the 20 sfu sunspot radio image at 1 GHz.** **a**: The input model of the radio ECM sources at 1 GHz displayed in a context of the sunspot and the corresponding gyroresonance opacity layer, similar to Fig. 4h in the main text. The model consists of a hundred randomly distributed point sources with a brightness temperature of 10^{11} K at selected field lines. **b**: similar Extended Data Fig. 4b in the main text, but showing the simulated VLA image at $\nu_{\text{GHz}} = 1.0$ overlaid on the HMI continuum intensity image.

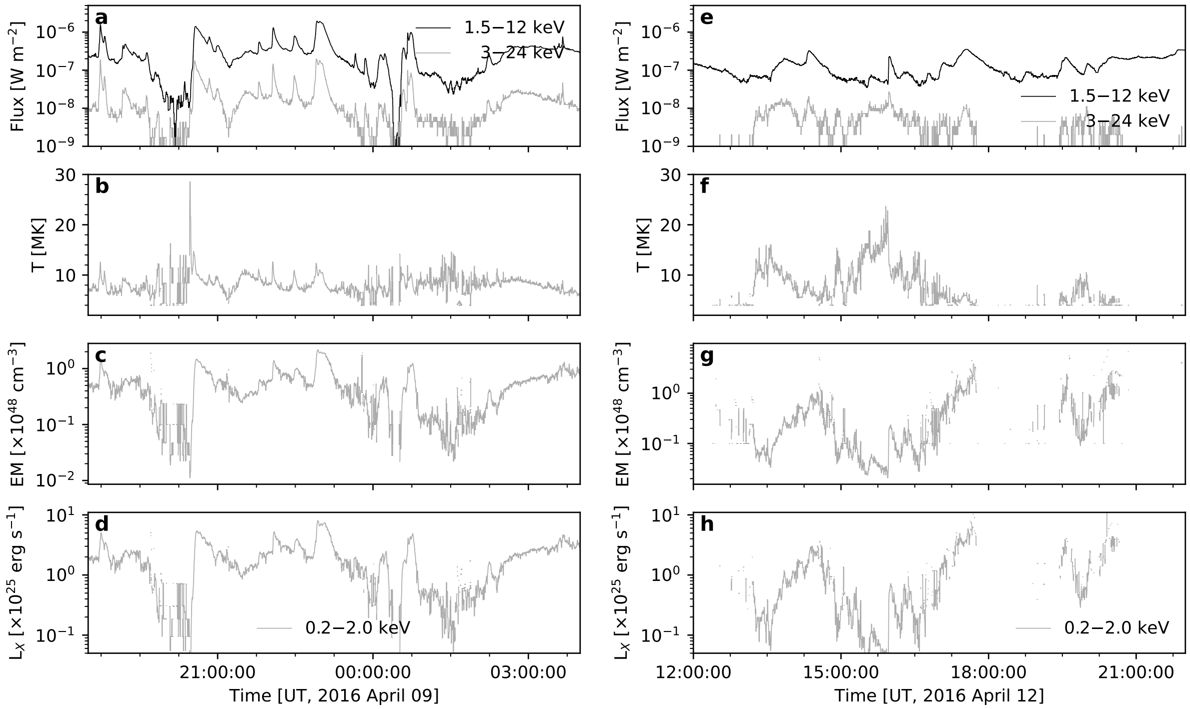

Supplementary Fig. 3. Temporal evolution of the flare activity in NOAA 12529 AR on April 9th (a–d) and 12th (e–h). Displayed sequentially from top to bottom are GOES 1.5–12 keV (black line) and 3–24 keV X-ray (grey line), the derived plasma temperature T and total emission measure EM determined based on the background-subtracted X-ray emission, as well as the X-ray luminosity in 0.2–2.0 keV (L_X) employing the Raymond-Smith plasma model.

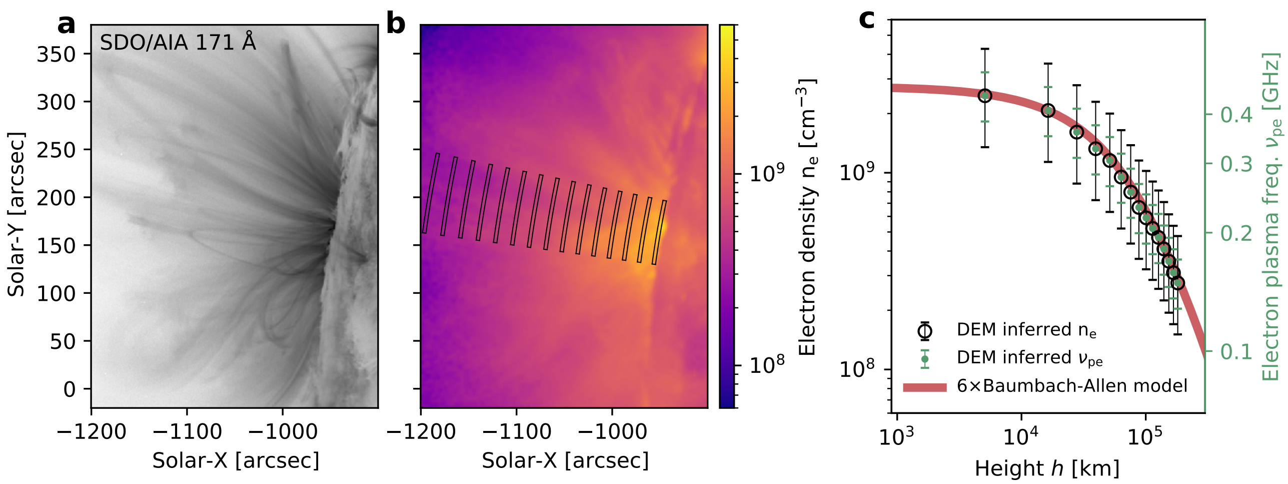

Supplementary Fig. 4. Electron number density distribution in the corona above the sunspot on 2016 April 7 when the sunspot was located at the east solar limb. a, SDO/AIA 171 Å passband image at 08:10 UT. **b**, electron density n_{e} derived by EUV diagnostics. **c**, distribution of n_{e} and the corresponding electron plasma frequency ν_{pe} in height h obtained from regions marked in (b) for a series of equally spaced radial heights above the sunspot. The red line represents the sixfold Baumbach–Allen model. The error bars are obtained by with the column depth D ranging from 15–150 Mm.

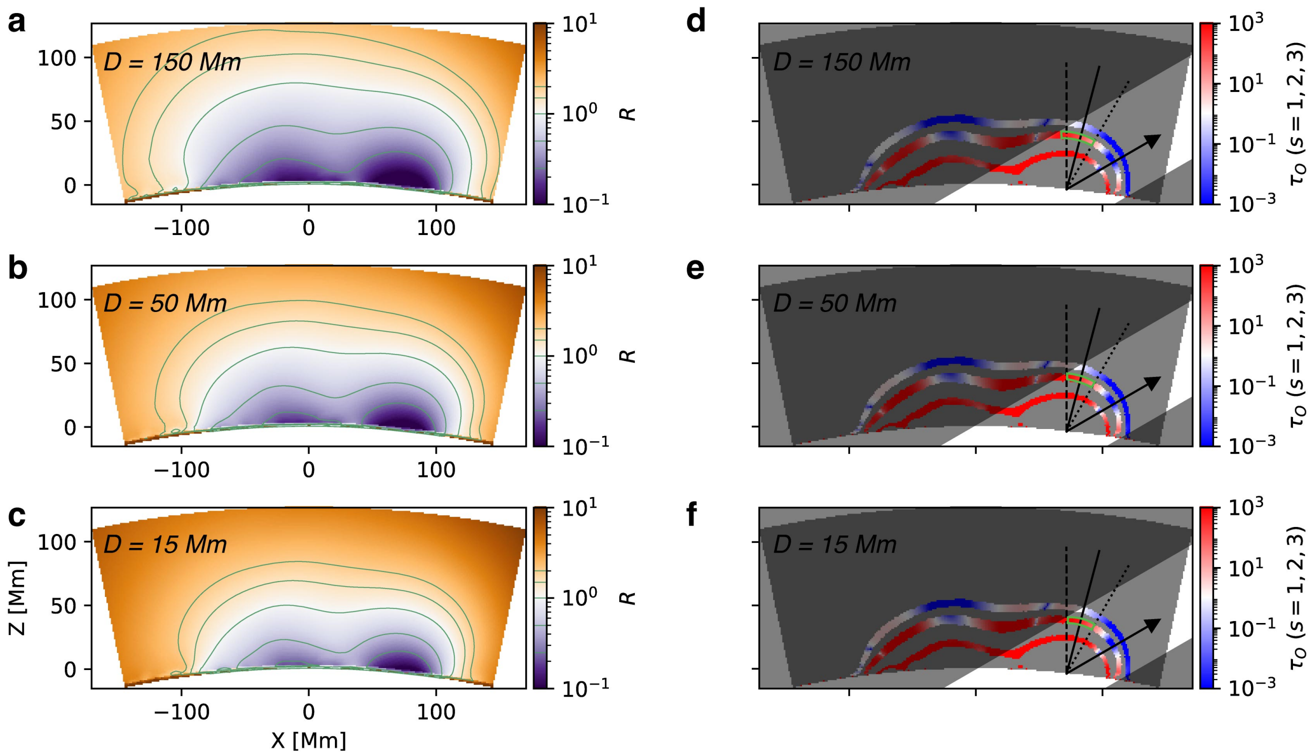

Supplementary Fig. 5. Physical characteristics in a 2D slice on the X–Z plane of the 3D model of NOAA 12529 AR for three different column depths. The left and right columns show the same plots of the ratio $R = \nu_{pe}/\nu_{ce}$ and the gyro-resonance opacity τ as Extended Data Fig. 5(c&f), but for column depths D of 150, 50, and 15 Mm from top to bottom, respectively.

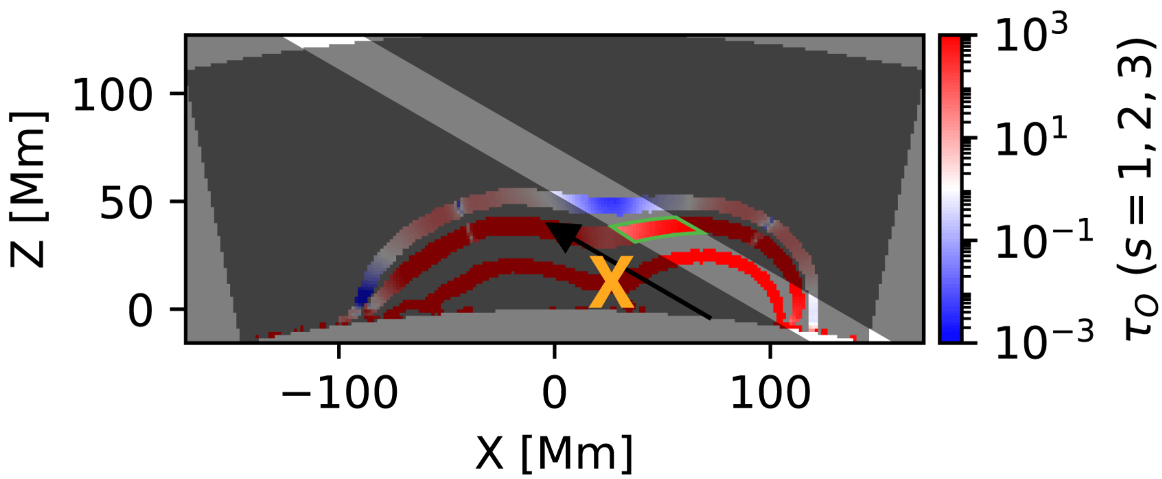

Supplementary Fig. 6. Gyro-resonance Opacity τ for O Mode Emission at $\nu_{GHz} = 1.0$. Contrary to the values derived from the line-of-sight in Extended Data Fig. 5(f), this representation considers the AR's position at the opposite longitude relative to the solar disk center. A 10-fold surge in electron number density n_e is assumed, accounting for the impact of the nearby flare region. The black arrow points toward the observer. The corona, transparent to the $s = 3$ gyro-resonance absorption layer, is highlighted by the slanted white shade. The green contour denotes the potential origin of the $s = 2$ ECM radio emissions, and the yellow cross pinpoints the solar flares' approximate location.

References

1. Hallinan, G. *et al.* Magnetospherically driven optical and radio aurorae at the end of the stellar main sequence. *Nature* **523**, 568–571 (2015).
2. Bastian, T. S., Cotton, W. D. & Hallinan, G. Radio Emission from UV Cet: Auroral Emission from a Stellar Magnetosphere. *Astrophys. J.* **935**, 99 (2022).
3. Zic, A. *et al.* ASKAP detection of periodic and elliptically polarized radio pulses from UV Ceti. *Mon. Not. R. Astron. Soc.* **488**, 559–571 (2019).
4. Villadsen, J. & Hallinan, G. Ultra-wideband Detection of 22 Coherent Radio Bursts on M Dwarfs. *Astrophys. J.* **871**, 214 (2019).
5. Melrose, D. B. & Dulk, G. A. Electron-cyclotron masers as the source of certain solar and stellar radio bursts. *Astrophys. J.* **259**, 844–858 (1982).
6. Wu, C. S. & Lee, L. C. A theory of the terrestrial kilometric radiation. *Astrophys. J.* **230**, 621–626 (1979).
7. Hess, S., Zarka, P. & Mottez, F. Io Jupiter interaction, millisecond bursts and field-aligned potentials. *Planet. Space Sci.* **55**, 89–99 (2007).
8. Lamy, L. *et al.* Saturn kilometric radiation: Average and statistical properties. *J. Geophys. Res. (Space Physics)* **113**, A07201 (2008).
9. Berger, E. *et al.* The Magnetic Properties of an L Dwarf Derived from Simultaneous Radio, X-Ray, and Hα Observations. *Astrophys. J.* **627**, 960–973 (2005).
10. Hallinan, G. *et al.* Periodic Bursts of Coherent Radio Emission from an Ultracool Dwarf. *Astrophys. J. Lett.* **663**, L25–L28 (2007).
11. Treumann, R. A. The electron-cyclotron maser for astrophysical application. *Astron. Astrophys. Rev.* **13**, 229–315 (2006).
12. Ergun, R. E. *et al.* Electron-Cyclotron Maser Driven by Charged-Particle Acceleration from Magnetic Field-aligned Electric Fields. *Astrophys. J.* **538**, 456–466 (2000).
13. Régnier, S. A new approach to the maser emission in the solar corona. *Astron. Astrophys.* **581**, A9 (2015).
14. Morosan, D. E., Zucca, P., Bloomfield, D. S. & Gallagher, P. T. Conditions for electron-cyclotron maser emission in the solar corona. *Astron. Astrophys.* **589**, L8 (2016).
15. Zlotnik, E. Y. Theory of the Slowly Changing Component of Solar Radio Emission. I. *Sov. Astron.* **12**, 245 (1968).
16. Winglee, R. M. Fundamental and harmonic electron cyclotron maser emission. *J. Geophys. Res.* **90**, 9663–9674 (1985).
17. Tong, Z.-J., Wang, C.-B., Zhang, P.-J. & Liu, J. A parametric investigation on the cyclotron maser instability driven by ring-beam electrons with intrinsic Alfvén waves. *Phys. Plasmas* **24**, 052902 (2017).
18. Chen, B. *et al.* Tracing Electron Beams in the Sun's Corona with Radio Dynamic Imaging Spectroscopy. *Astrophys. J. Lett.* **763**, L21 (2013).
19. Chen, B. *et al.* Magnetic Reconnection Null Points as the Origin of Semirelativistic Electron Beams in a Solar Jet. *Astrophys. J.* **866**, 62 (2018).
20. Hess, S., Mottez, F., Zarka, P. & Chust, T. Generation of the jovian radio decametric arcs from the Io Flux Tube. *J. Geophys. Res. Space Phys.* **113**, A03209 (2008).
21. Wu, C. S., Wang, C. B., Wu, D. J. & Lee, K. H. Resonant wave-particle interactions modified by intrinsic Alfvénic turbulence. *Phys. Plasmas* **19**, 082902 (2012).
22. McIntosh, S. W. *et al.* Alfvénic waves with sufficient energy to power the quiet solar corona and fast solar wind. *Nature* **475**, 477–480 (2011).
23. Grant, S. D. T. *et al.* Alfvén wave dissipation in the solar chromosphere. *Nat. Phys.* **14**, 480–483 (2018).
24. Yu, S. & Chen, B. Possible Detection of Subsecond-period Propagating Magnetohydrodynamics Waves in Post-reconnection Magnetic Loops during a Two-ribbon Solar Flare. *Astrophys. J.* **872**, 71 (2019).
25. Aschwanden, M. J. *Physics of the Solar Corona. An Introduction with Problems and Solutions (2nd edition)* (2005).
26. Cheung, M. C. M. *et al.* A comprehensive three-dimensional radiative magnetohydrodynamic simulation of a solar flare. *Nat. Astron.* **3**, 160–166 (2019).

27. Reeves, K. K., Warren, H. P. & Forbes, T. G. Theoretical Predictions of X-Ray and Extreme-UV Flare Emissions Using a Loss-of-Equilibrium Model of Solar Eruptions. *Astrophys. J.* **668**, 1210–1220 (2007).

28. Schmieder, B., Aulanier, G. & Vršnak, B. Flare-CME Models: An Observational Perspective (Invited Review). *Sol. Phys.* **290**, 3457–3486 (2015).

29. Robertson, P. *et al.* Persistent Starspot Signals on M Dwarfs: Multiwavelength Doppler Observations with the Habitable-zone Planet Finder and Keck/HIRES. *Astrophys. J.* **897**, 125 (2020).

30. Das, B. *et al.* Discovery of Eight "Main-sequence Radio Pulse Emitters" Using the GMRT: Clues to the Onset of Coherent Radio Emission in Hot Magnetic Stars. *Astrophys. J.* **925**, 125 (2022).

31. Berger, E. *et al.* Periodic Radio and Hα Emission from the L Dwarf Binary 2MASSW J0746425+200032: Exploring the Magnetic Field Topology and Radius Of An L Dwarf. *Astrophys. J.* **695**, 310–316 (2009).

32. Trigilio, C., Leto, P., Umana, G., Buemi, C. S. & Leone, F. Auroral Radio Emission from Stars: The Case of CU Virginis. *Astrophys. J. Lett.* **739**, L10 (2011).

33. Trigilio, C., Leto, P., Umana, G., Leone, F. & Buemi, C. S. A three-dimensional model for the radio emission of magnetic chemically peculiar stars. *Astron. Astrophys.* **418**, 593–605 (2004).

34. Kochukhov, O., Shultz, M. & Neiner, C. Magnetic field topologies of the bright, weak-field Ap stars θ Aurigae and Ursae Majoris. *Astron. Astrophys.* **621**, A47 (2019).

35. Leto, P. *et al.* Evidence for radio and X-ray auroral emissions from the magnetic B-type star ρ Oph A. *Mon. Not. R. Astron. Soc.* **493**, 4657–4676 (2020).

36. Kochukhov, O., Lüftinger, T., Neiner, C., Alecian, E. & MiMeS Collaboration. Magnetic field topology of the unique chemically peculiar star CU Virginis. *Astron. Astrophys.* **565**, A83 (2014).

37. Balona, L. A. *et al.* Rotational modulation in TESS B stars. *Mon. Not. R. Astron. Soc.* **485**, 3457–3469 (2019).

38. Cantiello, M. & Braithwaite, J. Magnetic spots on hot massive stars. *Astron. Astrophys.* **534**, A140 (2011).

39. Maeder, A. & Meynet, G. Stellar evolution with rotation and magnetic fields. II. General equations for the transport by Tayler-Spruit dynamo. *Astron. Astrophys.* **422**, 225–237 (2004).

40. Shultz, M. E. *et al.* The magnetic early B-type stars I: magnetometry and rotation. *Mon. Not. R. Astron. Soc.* **475**, 5144–5178 (2018).

41. Callingham, J. R. *et al.* The population of M dwarfs observed at low radio frequencies. *Nat. Astron.* **5**, 1233–1239 (2021).

42. Benz, A. O. Millisecond Radio Spikes. *Sol. Phys.* **104**, 99–110 (1986).

43. Bastian, T. S. Angular Scattering of Solar Radio Emission by Coronal Turbulence. *Astrophys. J.* **426**, 774 (1994).

44. Johns-Krull, C. M. & Valenti, J. A. Detection of Strong Magnetic Fields on M Dwarfs. *Astrophys. J. Lett.* **459**, L95 (1996).

45. Morin, J. *et al.* Large-scale magnetic topologies of late M dwarfs*. *Mon. Not. R. Astron. Soc.* **407**, 2269–2286 (2010).

46. Kochukhov, O. Magnetic fields of M dwarfs. *Astron. Astrophys. Rev.* **29**, 1 (2021).

47. Kao, M. M., Hallinan, G., Pineda, J. S., Stevenson, D. & Burgasser, A. The Strongest Magnetic Fields on the Coolest Brown Dwarfs. *Astrophys. J., Suppl. Ser.* **237**, 25 (2018).